J. Phys. Chem. B **2005,** *109,* 23001−23007

Direct Observation of Cations and Polynucleotides Explains Polyion Adsorption to Like-Charged Surfaces

Joseph A. Libera, Hao Cheng, Monica Olvera de la Cruz, and Michael J. Bedzyk*

Department of Materials Science and Engineering and The Nanoscale Science and Engineering Center, Northwestern University, Evanston, Illinois 60208

Received: June 27, 2005; In Final Form: September 11, 2005

We show an experimental approach for directly observing the condensation of polynucleotides and their electrolyte counterions at a liquid/solid interface. X-ray standing waves (XSW) generated by Bragg diffraction from a $d = 20$ nm Si/Mo multilayer substrate are used to measure the distinct distribution profiles of the polyanions and simple cations along the surface normal direction with subnanometer resolution. The 1D spatial sensitivity of this approach is enhanced by observing the XSW induced fluorescence modulations over multiple orders of Bragg peaks. We study the interesting divalent cation driven adsorption of anionic polynucleotides to anionic surfaces by exposing a hydroxyl-terminated silica surface to an aqueous solution with $ZnCl_2$ and mercurated poly-uridylic acid (a synthetic RNA molecule). The in situ long-period XSW measurements are used to follow the evolution of both the Zn and Hg distribution profiles during the adsorption process. The conditions and physical mechanisms that govern the observed divalent cation adsorption and subsequent polynucleotide adsorption to an anionic surface are explained by a thermodynamic model that incorporates nonlinear electrostatic effects.

Introduction

Biomolecular adsorption has crucial importance in science and in various technological processes including patterning,[1] biodetection,[2−4] and therapeutic delivery systems.[5] DNA or RNA adsorption onto a negatively charged surface in divalent metal ion solution has been widely used as a platform for further studies.[6,7] Adsorption of strongly charged polyanions to anionic surfaces via divalent cations could be controlled by pH and ionic strength if the adsorption mechanism were understood, providing a powerful tool for manipulating biomolecules. The understanding of the complex balance of energetic and entropic contributions that leads to adsorption cannot be improved unless the molecular and ionic distribution profiles are observed in situ simultaneously.

Strongly charged chains, such as DNA, are soluble in monovalent salt aqueous solutions because while cations are condensed along the chains to decrease the electrostatic energy, their overall charge is nonzero. Polyelectrolyte adsorption to oppositely charged surfaces[8] is due to the entropy gained by the release or partial release of surface and polyelectrolyte condensed counterions upon adsorption,[9] and is enhanced by lateral[10] and/or site-specific[11] correlations. When multivalent counterions are used to mediate polyelectrolyte adsorptions to like-charged surfaces, as in the binding of DNA to mica,[6,7,12] the adsorption mechanism is unclear. The ion translational entropy decreases upon adsorption given that more counterion condensation is required to annihilate the charge of the adsorbed layer. Moreover, the ionic correlations that in solution lead to the formation of neutral cation−polynucleotide aggregates within a range of multivalent cations (typically of valence $z \geq 3+$) and salt concentrations[13−18] cannot explain the divalent cation mediated adsorption. Strong multivalent cation mediated attractions among anionic chains and surfaces are in principle capable of leading to stable neutral surface−cation−chain complexes in the strongly correlated ionic limit, which requires high valence and density of adsorbed cations.[19−21] For high-valence cations, however, bulk chain precipitation is expected to preempt adsorption;[22] therefore, one should avoid $z > 2+$ and solution conditions that lead to cation−polynucleotide bulk precipitation.[23] By using $z = 2+$, we show here that the surface−cation−polynucleotide complex is not dense, suggesting another adsorption mechanism.

Models proposed to explain polynucleotide adsorption to like-charged surfaces include “ion-bridging” among the anionic surface and chain groups via divalent ions. In the dilute “bridging” limit a weakly charged surface would be required to overcome the electrostatic repulsion. If only electrostatic interactions are involved, the electrostatic energy of the bridging ions has to be equal to the chemical potential of the ions in the solution, which requires a large bulk concentration of cations contradicting the experiments. Therefore, unless there are strong site-specific interactions (chemical interaction) between the bridging ions and the surface and/or the chains, the model cannot explain adsorption. Site-specific interactions can in principle invert the charge of the chains and/or of the surface. Since polynucleotide adsorption to anionic surfaces works with some divalent cations, which do not necessarily invert the charge of DNA, for example, Mg^{2+},[24] the mechanism of DNA charge inversion before adsorption is not plausible. Surface charge inversion by the divalent cations in high divalent salt solutions[25] may explain the adsorption. However, as shown here, surface charge inversion is not a necessary condition for polynucleotide adsorption.

To address this question and more general adsorption questions one needs to observe the process in situ. Atomic-force microscopy (AFM) is useful for in situ studies of chain conformations adsorbed on surfaces. However, the verification

---

* Address correspondence to this Author. Phone: (847) 491-3570. Fax: (847) 467-2269. E-mail: bedzyk@northwestern.edu.

10.1021/jp0534941 CCC: \$30.25

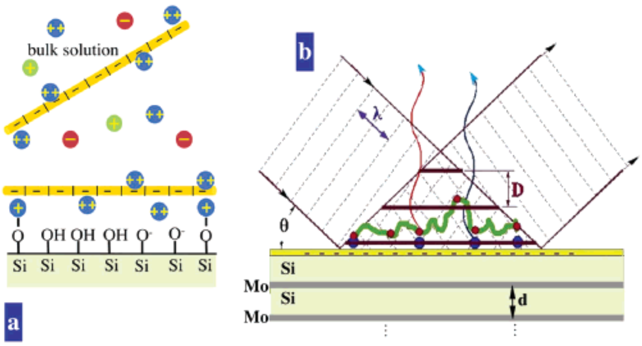

Figure 1. Depiction of the electrified interface and the X-ray standing wave. (a) Scheme for M^{2+} cation mediated electrostatic adsorption of a negatively charged polynucleotide to a negatively charged hydroxylated silica surface. (b) Depiction of X-ray standing wave (XSW) generated by Bragg diffraction from a Si/Mo multilayer mirror with period d. As the XSW period, D, and phase are experimentally adjusted by scanning the incident angle, θ, through a Bragg reflection, the element-specific X-ray fluorescence emission from ions on the surface (filled blue circles) and tag-atoms (filled red circles) attached to polyions near the surface will each modulate with a phase and amplitude that senses that particular atomic distribution profile $\rho(z)$.

of many predicted regimes of polyelectrolyte adsorption requires determination of the distribution along the surface normal for both the polyelectrolyte and counterions. Highly penetrating synchrotron X-rays are a natural choice for angstrom resolution studies in water. However, since there is typically no lateral ordering and there is poor electron density contrast between organic materials and water, standard in situ X-ray scattering techniques are largely insensitive for studying this type of interfacial system. We circumvent this problem by employing the long-period X-ray standing wave (XSW) method,[26−29] which only requires an X-ray reflecting substrate and X-ray fluorescence (XRF) detectable adsorbates (or tag atoms). As illustrated in Figure 1, this provides us with an in situ nanoprobe for studying the adsorption and conformation of polynucleotides and cations at a charged surface.

We examined the adsorption of mercurated poly(U) in a $ZnCl_2$ aqueous solution to a hydroxylated SiO_x surface. Poly(U) was chosen to avoid complications arising from the native conformation of RNA. Zn was chosen because Zn^{2+} does not have strong specific interactions with poly(U)[30] and therefore does not precipitate the chains in the bulk nor does it lead to charge inversion of the polynucleotides in solution.

Materials and Methods

Sample Preparation. Polyuridylic acid(5′) potassium salt (2380−2900 units) (poly(U)) was obtained from Sigma Chemical Co. (St. Louis, MO) and labeled with one Hg atom per unit following the method of Dale et al.[31] Referring to Figure 1, the adsorption surface was the SiO_x (silica) top surface of the final Si layer of a 20-layer pair Si/Mo layered-synthetic-microstructure (LSM) X-ray mirror. The LSM mirrors were made at the Advanced Photon Source Optics Facility by DC magnetron sputter deposition on Si substrates (37.5 mm long by 12.5 mm wide by 2.5 mm thick). The Si/Mo multilayer periodicity (d spacing) was determined to be $d = 18.5$ nm by X-ray reflectivity (XRR) analysis, with details given elsewhere.[32] Immediately prior to the X-ray measurements, the surface was cleaned by piranha solution (2:1, sulfuric acid:hydrogen peroxide) and then hydroxylated by 3 M HCl. Prior to and following each of these steps the sample was rinsed with Millipore water and dried under a stream of N_2 gas.

X-ray Measurements. The X-ray measurements were performed in a thin film reflection geometry at the European Synchrotron Radiation Facility (ESRF) ID32 beamline, using an incident photon energy of $E_\gamma = 12.40$ keV (corresponding to a wavelength of $\lambda = 1.000$ Å). The photon flux through the 0.015-mm high by 1.0-mm wide incident beam slit was 2×10^{11} p/s. The sample was sealed inside a liquid−solid interface cell with a 7-μm thick Kapton X-ray window lying parallel to and above the sample surface. After injection the test aqueous solution was trapped between the sample surface and the Kapton. The aqueous layer was held at an expanded volume for 1 h of incubation and then contracted to form a 2−3 μm uniformly thick layer during the X-ray measurements. The X-ray beam passed through the Kapton and water layers establishing the XSW in the test solution above the substrate surface. The water and Kapton layers refract and partially absorb the incoming and outgoing X-ray beams. This becomes an increasingly significant effect at the small incident angles of $\theta < 1°$ used for these measurements.

In the XSW measurement the X-ray specular reflectivity (R) and fluorescence data were simultaneously collected in a $\theta-2\theta$ scan covering the range of the first three Bragg peaks of the LSM mirror. X-ray fluorescence spectra were collected in a multichannel analyzer (MCA) at each angle step of the scan, using an energy-dispersive Rontec silicon drift-diode detector (SDD). To produce the XRF yields the MCA net counts in the Zn and Hg peaks were extracted by appropriate curve fitting, corrected for dead-time effects, and corrected for variations in the length of the X-ray beam footprint. The Zn and Hg absolute (depth-integrated) atomic density, n_T, was obtained by XRF comparison of the Zn Kα and Hg Lα yields to the As Kα yield of an arsenic implanted Si substrate that had a Rutherford backscattering spectroscopy (RBS) calibrated coverage. This determination used sensitivity factors for relative emission rates of each of the XRF signals,[33] and also accounted for the Kapton and water attenuation of the incident X-ray beam and out-going fluorescence X-rays.

Long-period X-ray standing wave (XSW) analysis is generally used for measuring element-specific atomic distribution profiles $\rho(z)$ in a surface overlayer structure. In the present case, the XSW was generated by a reflection from a periodic layered synthetic microstructure (LSM).[26,32,34] The underlying formalism for describing the E-fields at the LSM interfaces and the subsequent E-field intensities and reflectivity is based on Parratt's recursion formulation.[35] Referring to Figure 1b, the XSW E-field intensity $I(\theta,z)$, which is produced by the interference between the incident and reflected X-ray plane waves, has planes of equal intensity (nodes and antinodes) that are parallel to the LSM interfaces. (We choose the z-direction to be perpendicular to this set of parallel interfaces.) In the vacuum (or air) region above the reflecting surface, the normalized E-field intensity is

$$I(q,z) = 1 + R + 2\sqrt{R}\cos(\upsilon - qz) \qquad (1)$$

and consequently the XSW period is

$$D = \lambda/2 \sin\theta = 2\pi/q \qquad (2)$$

where $q = 4\pi (\sin\theta)/\lambda$ is the magnitude of the wavevector transfer, R is the reflectivity, and υ is the XSW phase.

Bragg's law ($m\lambda = 2d \sin\theta_m$), which simply considers geometry, can be used to approximately find where the Bragg peaks should occur in a $\theta-2\theta$ specular scan. However, due to strong refraction effects that occur at small angles, the mth-order Bragg peak will be shifted slightly higher than the geometrical Bragg angle, θ_m. Due to the finite "effective" number of periods in the LSM, each Bragg peak will occur over a finite angular width, over which, the reflectivity and XSW fringe visibility will be dramatically enhanced. Furthermore, increasing the incident angle through a Bragg reflection causes the phase (v) of the XSW to shift inward by one-half of its period. Since the photoelectric effect cross-section (in the dipole approximation) is proportional to the E-field intensity at the center of an atom, this phase shift induces a modulation in the X-ray fluorescence (XRF) yield from a given atom that is characteristic of the spatial distribution profile $\rho(z)$ for that atomic species. In general, narrower distributions will produce larger modulation amplitudes. The XRF yield from an atomic layer that is positioned in-phase with the diffraction planes will have a minima on the low-angle side and a maxima on the high-angle side of the Bragg peak, and visa versa for an atom layer aligned midway between diffraction planes.

The method for quantitatively extracting the atomic distribution profile $\rho(z)$ from the XSW data starts with determining the thicknesses, indices of refraction, and interfacial widths of all the layers by analysis[35] of the reflectivity data. This "effective" electron density profile for the LSM, water, and Kapton layers is then used in calculating the E-field intensity, $I(q,z)$, above the LSM surface, which in turn is used for simulating the XRF yield

$$Y(q) = \int \rho(z) I(q,z)\, \mathrm{d}z \tag{3}$$

for the unknown Zn or Hg atomic distribution profile $\rho(z)$. Further details of this XSW analysis procedure can be found elsewhere.[32,36]

This ability to generate a variable period XSW over a range allows one to measure atomic distributions over these same length scales. In essence, the measured modulations in the element-specific fluorescence yield lead to a measure of the amplitude and phase of the Fourier transform $F(q)$ of the distribution $\rho(z)$ of that atom.

Results

Figure 1 illustrates the adsorption process and the method for generating the XSW by Bragg diffraction from the supporting $d = 18.5$ nm periodic Si/Mo multilayer substrate. The initial silica adsorption surface is expected to have a surface hydroxyl density of $n_S \sim 5\ \mathrm{nm}^{-2}$.[37] Sample **A** was processed with only the 50 μM $ZnCl_2$ solution. Sample **B** was processed with a solution that was 50 μM $ZnCl_2$ and 25 μM Hg-poly(U). These nominal concentrations were chosen to induce adsorption, discern the possible mechanism of Zn^{2+} mediated adsorption, and have sufficient signal contrast from the amount of Zn (or Hg) in the condensed surface layer in comparison to the amount contained in the 2−3 μm of bulk solution. (On the basis of inductively coupled plasma (ICP) spectroscopy, sample **B** also had 150 μM NaCl left over from the Hg-poly(U) preparation. The Na and Cl XRF signals are too low in energy to be detected through the water and Kapton.)

As depicted in Figure 1b, the superposition of the Bragg diffracted X-ray plane wave with the incident plane wave produces a XSW above the reflecting surface with a period (in air) defined by eq 2. The XSW has a sufficiently strong intensity modulation (as described in eq 1) for use as a 1D XRF nanoprobe, when the reflectivity (R) is greater than 10%. For our present case, we use the 1st-, 2nd-, and 3rd-order Bragg peaks, which can be seen in the X-ray reflectivity (XRR) data and simulations shown in Figure 2a. Over this q-range the XSW period in the air above the LSM decreases continuously from 15.8 to 4.8 nm. The corresponding value of D at each Bragg peak is listed above each peak in Figure 2a.[38] In addition to this continual contraction of the XSW period, the XSW also undergoes an inward 180° phase shift when advancing through each Bragg peak. Thus the element-specific XRF yield, $Y(q)$, from a layer of atoms lying above the LSM surface will modulate in a manner that is directly dependent on that layer's distribution profile, $\rho(z)$, as measured along the surface normal direction, z.

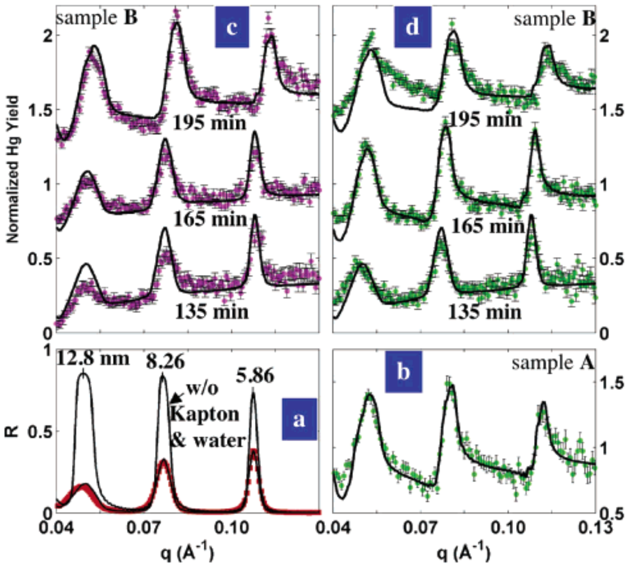

Figure 2. X-ray standing wave data and analysis. (a) Measured and calculated X-ray reflectivity (R) from the $d = 18.5$ Å LSM for a $\theta-2\theta$ scan through the 1st-, 2nd-, and 3rd-order Bragg peaks. Also shown is the reflectivity without the Kapton and water layers. (b−d) Measured and calculated XSW normalized Zn Kα and Hg Lα fluorescence yields collected simultaneously with R. (b) Sample **A** Zn yield. (c and d) Time sequence for the Hg and Zn yields of sample **B**. The yields in panels c and d are vertically offset for clarity: the 135 min data are displaced downward and the 195 min data are displaced upward.

For reasons of simplicity we use a step-function model for the Zn distribution profile, $\rho(z)$, that has a narrow condensed layer just above the silica surface followed by a bulk solution layer. The two model parameters determined by the fit to the XSW fluorescence yield data are C, the fraction of Zn atoms contained within the condensed layer, and t, the condensed layer thickness. The Zn total (depth-integrated) atomic density, n_T, was also determined with the same experimental setup by XRF comparison to a calibrated standard. For sample **A** the χ^2 fit of the modeled yield (eq 3) to the data is shown in Figure 2b and the fit determined values are listed in Table 1 along with values from a follow-up measurement taken at a fresh (unradiated) spot on the sample surface.

The adsorption process of Hg-poly(U) was studied by six successive XSW scans at 30-min intervals of sample **B.** To minimize (and to rule out) X-ray induced photochemical effects, we moved the several mm^2 X-ray footprint to a fresh (unradiated) spot after the second and fourth scans. Panels c and d of Figure 2 show the Hg Lα and Zn Kα fluorescence yields for the third, fourth, and fifth scans. (The first two scans (not displayed) match the third, and the sixth matches the fifth.) The time duration for each data set in Figure 2c,d was 17.5 min. Both the Zn and Hg time sequence of yield curves show pronounced changes. Such a change on this time scale did not occur for sample **A**, where poly(U) was absent. We used the

TABLE 1: Time Dependence of X-ray Determined Values[a]

		Zn					Hg				
time, min	t_W, μm	n_T, nm^{-2}	C	t, nm	n_S, nm^{-2}	[Zn], μM	n_T, nm^{-2}	C	t, nm	n_S, nm^{-2}	[Hg], μM
					sample **B**						
75	2.8	0.08	0		0	48	0.19	0		0	110
105	3.0	0.09	0		0	49	0.22	0		0	119
135	3.1	0.12	0		0	64	0.07	0		0	38
165	2.5	0.10	0.46	1.1	0.047	38	0.08	0		0.008	47
195	3.0	0.11	0.35	0.9	0.038	40	0.08	0.59	1.9	0.040	24
225	3.0	0.11	0.39	1.0	0.045	38	0.08	0.52	1.6	0.032	28
					sample **A**						
75	2.4	0.06	0.59	1.1	0.037	17					
165	2.4	0.06	0.44	0.9	0.027	25					

[a] Time = 0 corresponds to the initial exposure of the hydroxylated silica surface to the solution. XRR analysis (Figure 2a) determines the water layer thickness (t_W). Calibrated XRF analysis determines the total (depth-integrated) atomic density (n_T). XSW analysis (Figure 2b−d, Figure 3, and eq 3) determines the fraction (C) of Zn (or Hg) condensed at the surface and the condensed layer thickness (t). From these measured values we calculate the surface atomic density of the condensed layer, $n_S = Cn_T$, and the X-ray measured bulk solution concentration, $[x] = (1 - C)n_T/t_W/N_A$.

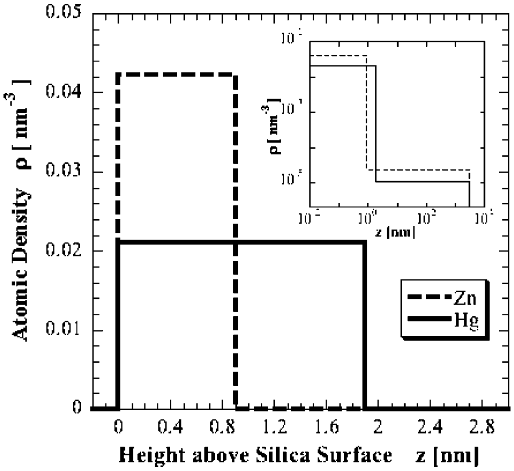

Figure 3. Step-function model for Zn and Hg atomic distribution profiles. The model includes a very thin condensed layer at the liquid/solid interface followed by a very dilute bulk-solution layer with thickness $t_w = 3\ \mu$m determined by X-ray reflectivity. These particular curves correspond to the models used in eq 3 that produced the best-fit yield curves to the data taken at 195 min shown in panels c and d of Figure 2 with values listed in Table 1. The inset shows a log−log plot over the entire range of the water layer thickness.

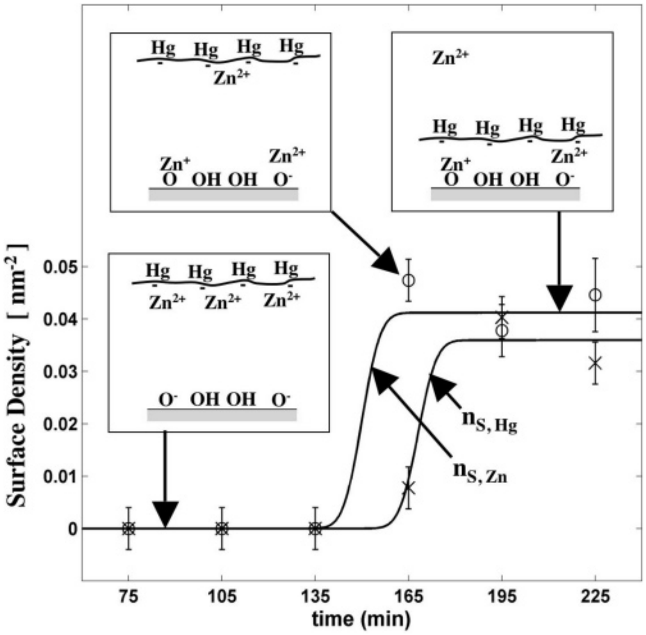

Figure 4. X-ray standing wave observed cation and polyanion adsorption process. The time dependence of the Zn (circles) and Hg (crosses) surface condensed layer densities. The lines are drawn to guide the eye. The insets depict the ion (and polyion) configurations at the various stages of the adsorption process.

same model as described above for modeling both the Zn and Hg atomic distribution profiles to determine the modeled yields shown in Figure 2c,d with the fit determined parameters listed in Table 1 for all six scans.[39] Here we see that there is no measurable adsorption of Zn or Hg-poly(U) for the first 135 min after the initial exposure to the solution. The first change in the system occurred after 165 min where we observe a condensed Zn layer with $C_{Zn} = 0.46$ and $t_{Zn} = 1.1$ nm, which is very similar to the condensed Zn layer of sample **A**. At this same time we also find a small change in the Hg yield suggesting the onset of Hg-poly(U) condensation. At 195 min we observe condensed layers for both the Zn and Hg-poly(U). The models for the Zn and Hg atomic distribution profiles at the 195-min stage of the process are shown in Figure 3. We see that the thickness of the Hg layer is twice as thick as the Zn layer and that the centroid of the Hg condensed layer is 0.5 nm higher than that of the Zn. This is consistent with the Zn being sandwiched between the poly(U) and the hydroxylated surface as depicted in Figure 1a. (Note that including a vertical offset $\langle z \rangle$ in the model of the condensed layer as an additional fitting parameter did not significantly improve χ^2.) The data are most sensitive in determining the surface density of the condensed layer (n_S), which is also listed in Table 1 and plotted as a function of time in Figure 4. Note that after reaching equilibrium the Hg and Zn surface densities match up and are at 1% of the expected surface hydroxyl density for the starting surface.

After the in situ measurements sample **B** was rinsed with Millipore water and blown dry with N_2. The XRF analysis of the dried sample showed a Zn density reduced to $n_T = 0.004 \pm 0.001$ nm^{-2} and no measurable Hg, indicating that the poly(U) was physically adsorbed.

Discussion

To explain these observations we extended a two-state model developed to analyze polyelectrolyte adsorption to surfaces with a fixed charge densities[11] to the case of divalent and polynucleotide adsorption to surfaces with weak (ionizable) charge groups. In the two-state model we assume two possible thermodynamic states for all of the chemical species: adsorbed and in bulk solution. The chemical components in these two states are in equilibrium. This is a standard way to treat surface or interface adsorption in multicomponent solutions.[40] In charged systems, the two-state model has been used to describe successfully adsorption of ions around charged colloids,[41] charged rods,[42] and finite size charged chains of different fractal geometries.[43] The two-state model is equivalent to the solution of the nonlinear Poisson−Boltzmann equations when short-range correlations are ignored, and has the advantage of being able to include short-range correlations. Our two-state model involves surface silanol group ionization and the reaction between divalent metal ions and silanol groups,

$$-\text{SiOH} + \text{H}_2\text{O} \rightleftharpoons -\text{SiO}^- + \text{H}_3\text{O}^+ \tag{4}$$

$$-\text{SiOH} + \text{M}^{2+} + \text{H}_2\text{O} \rightleftharpoons -\text{SiOM}^- + \text{H}_3\text{O}^+ \tag{5}$$

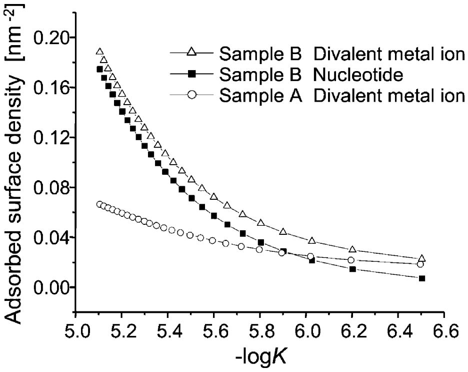

Figure 5. Calculated variation of nucleotide and divalent metal ion adsorption onto silica surface as a function of the association constant. The following experimental parameters are used: For sample **A** the parameters are [$ZnCl_2$] = 17 μM, pH 6.7, a 0.45 nm hydrated ion radius, 1 nm Zinc layer thickness, pK_a = 7.2, and 5 nm^{-2} silanol group surface density. For sample **B** the additional parameters are [$ZnCl_2$] = 40 μM, [NaCl]= 150 μM, 25 μM nucleotide concentration, the distance between neighboring charged nucleotides is 0.45 nm, the diameter of polynucleotide is 1 nm, and the polymerization degree of polynucleotide is 2500.

The dissociation constant K_a of the reaction in eq 4 is pK_a = $-$logK_a = 7.2.[44] The association constant K of the reaction in eq 5 varies with different kinds of divalent metal ions: available values of pK = $-$logK range from 8.1 for Mg^{2+} to 5.1 for Pb^{2+}.[45] For simple divalent salt solutions (sample **A**), the densities of $-SiO^-$, $-SiOM^+$, and unreacted condensed M^{2+} at the surface are functions of the bulk concentrations of M^{2+} and of H^+ where $[H^+]_{bulk} = 10^{-pH}$. These surface densities are determined self-consistently by minimizing the total free energy of the system, which includes contributions from entropy, electrostatics, and $-\ln K_a$ and $-\ln K$ energy changes due to the reactions described in eqs 4 and 5. After minimizing the total free energy, we get

$$\frac{[-SiO^-]_s[H_3O^+]_s}{[-SiOH]_s} = K_a \exp(\overline{\psi_s}) \tag{6}$$

$$\frac{[-SiOM^+]_s[H_3O^+]_s}{[-SiOH]_s[M^{2+}]_s} = K \exp(-\overline{\psi_s}) \tag{7}$$

where the subscription "s" in eqs 6 and 7 refers to the concentration on the surface or surface densities. $\overline{\psi_s} = e\psi_s/k_BT$ is the reduced surface potential and is a function of component surface densities. These surface densities can be determined after further self-consistent calculation. For Zn^{2+} we expect pK to be slightly greater than 5.5, the value for Cu^{2+}.[44,45] The prediction in Figure 5 then reasonably matches the degree of adsorption experimentally observed for sample **A** (listed as n_S in Table 1). This result (sample **A** in Figure 5) obtained with the two-state model also can be obtained by a modified one-dimensional nonlinear Poisson−Boltzmann approach, the site-binding model,[46] which has been extensively used to include specific short-range interactions among adsorbed divalent ions and surfaces as in our case. We next include the polyelectrolyte and NaCl in the solution and determine the adsorption of Zn and poly(U) at the surface in equilibrium with the bulk solution. The free Zn^{2+} concentration and the reduced surface potential in eqs 6 and 7 are modified in the presence of polynucleotides with condensed counterions. To determine the degree of polynucleotide adsorption we modified a previously proposed two-state model.[11] The model includes ion condensation along the chains, and short-range attractions among the surface charged groups and the charged units along the adsorbed chains. Our present study has the extra constraint that the surface-charged density is to be determined self-consistently rather than to assume it is a constant with a fixed value independent of the pH value, and of the salt and polynucleotide concentrations. The short-range interaction in our present study is the chemical reactions of divalent metal ions with surface groups. We assume here a uniformly charged layer on the surface, which includes the charges from $-SiO^-$, $-SiOM^+$, M^{2+}, Na^+, and polynucleotides. That is, contrary to the assumption in ref 11, the monovalent and divalent condensed ions on the adsorbed chains are not confined to the chain backbone but rather are smeared on the surface because in the present study the divalent ions that partially compensate for the charge of the adsorbed polynucleotides can react with the surface via eq 5 and the monovalent ions can also be electrostatically attracted to the surface. The two-state model used here allows us to incorporate the correlation and other effects in the adsorption of charged chains, providing a convenient method to study polymer adsorption and assembly.[11] The self-consistent results of polynucleotide solution for sample **B** described in Figure 5 are obtained by minimizing the resulting free energy. In Figure 5 if we choose (as argued earlier) a pK slightly greater than 5.5 for Zn^{2+}, then we see that the values predicted from our theory are in reasonable agreement with our experimentally determined values for sample **B** (listed as n_S in Table 1).

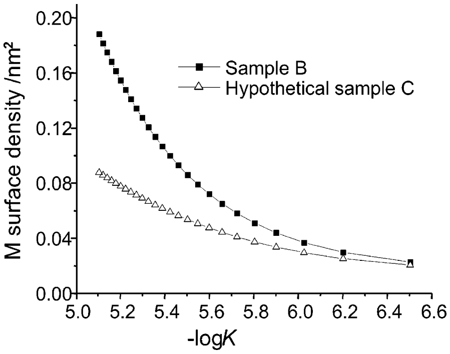

Figure 6. Theoretical comparison of total divalent metal ion (M) surface coverage for solutions with and without poly(U). Hypothetical sample **C** has the same amount of free divalent ions and sodium ions in the bulk solution as sample **B**, but without poly(U) adsorption. More divalent ions adsorb onto the surface to cancel the charge of adsorbed poly(U). For the condition of larger pK, less poly(U) is adsorbed. Therefore, the difference of M surface coverage between sample **B** and hypothetical sample **C** in this limit decreases.

We conclude that the in situ XSW observed adsorption of Zn and poly(U) is due to the binding of Zn^{2+} to silica to form $-SiOZn^+$ groups at the surface and a cooperative effect. When poly(U) with its condensed Zn^{2+} approaches the nearly neutralized negatively charged surface, the surface Zn^{2+} concentration increases and the reaction in eq 5 is promoted forming $-SiOZn^+$ which generate a net attraction force between the like-charged surface and polynucleotides. Though more Zn at the surface is required for poly(U) adsorption than without poly(U), in samples **A** and **B** the adsorbed Zn surface densities are comparable. This is due to the presence of NaCl in sample **B** and due to the different values of the free Zn in the bulk (a fraction of the measured bulk Zn^{2+} is condensed on the poly(U) in the bulk solution). When we compare the degree of adsorption of Zn in a hypothetical sample **C** with the same conditions as **B** but without adsorbed poly(U), we get much less Zn adsorption (Figure 6). This comparison can prove the widely accepted opinion that when polynucleotides adsorb onto an anionic surface, extra divalent ions need to be condensed onto the surface to neutralize the charge. The addition of NaCl leads to less overall adsorption of both poly(U) and Zn.

Our model predicts the degree of adsorption for various surfaces and/or divalent ions. For fixed concentrations of strong polyelectrolytes whose charges are not strongly pH dependent, such as polynucleotides, and fixed salt concentration, there is a critical K value of the reaction in eqs 5 and 7, denoted by K^c, such that for $K < K^c$, there is no polyelectrolyte adsorption to like-charge surfaces. This limiting K^c is obtained by minimizing the total free energy and is given by $K^c \approx -A[H^+]_{bulk} + BK_a$, where K_a is defined in eq 6, and A and B are positive constants. This result is obtained by assuming that the variation of pH from 6 to 8 does not change the screening length, which is dominated by salt concentration, and that the polyelectrolyte charge is pH independent in this pH range. That is, the chemical potentials of the polyelectrolytes in bulk or on the surface are constant and therefore $\overline{\psi_s}$ is constant and included in A and B. Notice that $-[H^+]_{bulk}/K_a$ is the ability to produce negative charges on the surface, and K/K_a is the association constant of the reaction creating positive charges on the surface via $-SiO^- + M^{2+} \Leftrightarrow SiOM^+$. Therefore, our model suggests that it is easier to adsorb strong polyanions onto a negatively charged surface if the surface groups are hard to ionize and if they interact more strongly with the divalent metal ions. The ability to form negative or positive charges involves the effective surface electrostatic potential in A and B, which are determined by the charge density of the polyelectrolyte and salt concentration.

Referring to Figure 4 the sluggish adsorption kinetics in sample **B** suggests a delicate balance of forces. Since the charge of poly(U) is only partially neutralized, it may take a long time for poly(U) to approach a negatively charged surface. In another set of XSW experiments for this same system, we added in a $ZnCl_2$(aq) surface pretreatment step into the sample preparation that occurred just prior to injection of the Hg-poly(U) and $ZnCl_2$ solution. In this pretreatment step the surface was triply flushed with and then incubated for 20 min in 50 μM $ZnCl_2$. The XSW measurement that took up a 30 min time interval after this injection showed Hg-poly(U) and Zn adsorption had occurred much more quickly than in the case of sample **B**. This faster adsorption process appears to be related to the surface charge being highly neutralized by the zinc pretreatment.

Conclusions

We show by following simultaneously the counterion and polyion distribution profiles during their adsorption process that charged macromolecules affect significantly the equilibrium concentration of ions reacting with the surface. The induced equilibrium shift is shown to strongly influence the interactions among the surface and the polyions. Our observations and model demonstrate that polynucleotide adsorption to a like charge surface via divalent ions in virtue of a cooperative effect does not require the bridging mechanism of the Zn^{2+} to both the surface and the nucleotide, nor the charge inversion of the surface or of the polynucleotide. Our model, constructed from XSW experimental observations, points to the importance of determining self-consistently the number density of reacting multivalent metallic ions with weakly charged groups along macroions or surfaces in order to determine the interactions with strongly charged polyions which have nearly pH-independent charge densities.

Our approach should be useful in the study of polynucleotide and protein interactions[47] and DNA or RNA delivery into negatively charged cell membranes. Our experimental method represents a unique capability that can be applied to study the kinetics and equilibrium structure for a wide range of phenomena related to biomolecular adsorption, including DNA and other types of polyions in aqueous solution. Furthermore, the experimental method can be used to solve important polyelectrolyte adsorption questions such as the degree of charge inversion[48,49] and ionic correlations[50] in various ionic media.

Acknowledgment. We gratefully acknowledge helpful discussions with P. Fenter, A. Mondragon, and C. Mirkin, and technical assistance from K. Zhang, Z. Zhang, T.-L. Lee, J. Zegenhagen, C. Cohen, L. Andre, C. Liu, and R. Conley. This work was supported by the National Institutes of Health (GM62109-02), National Science Foundation (EEC-0118025 and DMR-0076097), Department of Energy (W-31-109-Eng-38), and the European Synchrotron Radiation Facility.

References and Notes

(1) Jiang, X. Y.; Xu, Q. B.; Dertinger, S. K. W.; Stroock, A. D.; Fu, T. M.; Whitesides, G. M. *Anal. Chem.* **2005**, *77*, 2338−2347.

(2) Nam, J. M.; Thaxton, C. S.; Mirkin, C. A. *Science* **2003**, *301*, 1884−1886.

(3) Ghosh, D.; Ramakanth, M.; Bhaumik, A.; Faure, N.; Rondelez, F.; Chatterji, D. *J. Biochem. Biophys. Methods* **2005**, *62*, 51−62.

(4) Bustamante, C.; Bryant, Z.; Smith, S. B. *Nature* **2003**, *421*, 423−427.

(5) Radler, J. O.; Koltover, I.; Salditt, T.; Safinya, C. R. *Science* **1997**, *275*, 810−814.

(6) Kasas, S.; Thomson, N. H.; Smith, B. L.; Hansma, H. G.; Zhu, X. S.; Guthold, M.; Bustamante, C.; Kool, E. T.; Kashlev, M.; Hansma, P. K. *Biochemistry* **1997**, *36*, 461−468.

(7) van Noort, S. J. T.; van der Werf, K. O.; Eker, A. P. M.; Wyman, C.; de Grooth, B. G.; van Hulst, N. F.; Greve, J. *Biophys. J.* **1998**, *74*, 2840−2849.

(8) Netz, R. R.; Andelman, D. *Phys. Rep.* **2003**, *380*, 1−95.

(9) Sens, P.; Joanny, J.-F. *Phys. Rev. Lett.* **2000**, *84*, 4862−4865.

(10) Dobrynin, A. V.; Deshkovski, A.; Rubinstein, M. *Macromolecules* **2001**, *34*, 3421−3436.

(11) Cheng, H.; Olvera de la Cruz, M. *J. Polym. Sci. Part B*: *Polym. Phys.* **2004**, *42*, 3642−3653.

(12) Hansma, H. G.; Laney, D. E. *Biophys. J.* **1996**, *70*, 1933−1939.

(13) Widom, J.; Baldwin, R. L. *J. Mol. Biol.* **1980**, *144*, 431−453.

(14) Bloomfield, V. A. *Curr. Opin. Struct. Biol.* **1996**, *6*, 334−341.

(15) Solis, F. J.; Olvera de la Cruz, M. *Eur. Phys. J. E* **2001**, *4*, 143−152.

(16) Allahyarov, E.; Lowen, H.; Gompper. *Europhys. Lett.* **2004**, *68*, 894−900.

(17) Liu, S.; Ghosh, K.; Muthukumar, M. *J. Chem. Phys.* **2003**, *119*, 1813−1823.

(18) Raspaud, E.; Olvera de la Cruz, M.; Sikorav, J. L.; Livolant, F. *Biophys. J.* **1998**, *74*, 381−393.

(19) Stevens, M. J.; Robbins, M. O. *Europhys. Lett.* **1990**, *12*, 81−86.

(20) Rouzina, I.; Bloomfield, V. A. *J. Chem. Phys.* **1996**, *100*, 9977.

(21) Kjellander, R.; Ajesson, T.; Jonson, B.; Marcelja, S. *J. Chem. Phys.* **1992**, *97*, 1424−1431.

(22) Messina, R.; Holm, C.; Kremer, K. *J. Chem. Phys.* **2002**, *117*, 2947−2960.

(23) Rau, D. C.; Parsegian, A. V. *Biophys. J.* **1992**, *61*, 260−271.

(24) Das, R.; Mills, T. T.; Kwok, L. W.; Maskel, G. S.; Millett, I. S.; Doniach, S.; Finkelstein, K. D.; Herschlag, D.; Pollack, L. *Phys. Rev. Lett.* **2003**, *90*, 188103.

(25) Kekicheff, P.; Marcelja, S.; Senden, T. J.; Shubin, V. E. *J. Chem. Phys.* **1993**, *99*, 6098−6113.

(26) Bedzyk, M. J.; Bilderback, D. H.; Bommarito, G. M.; Caffrey, M.; Schildkraut, J. S. *Science* **1988**, *241*, 1788−1791.

(27) Bedzyk, M. J.; Bommarito, G. M.; Caffrey, M.; Penner, T. L. *Science* **1990**, *248*, 52−56.

(28) Templeton, A. S.; Trainor, T. P.; Traina, S. J.; Spormann, A. M.; Brown, G. E. *Proc. Natl. Acad. Sci*. **2001**, *98*, 11897−11902.

(29) Libera, J. A.; Gurney, R. W.; Schwartz, C.; Jin, H.; Lee, T. L.; Nguyen, S. T.; Hupp, J. T.; Bedzyk, M. J. *J. Phys. Chem. B* **2005**, *109*, 1441−1450.

(30) Izatt, R. M.; Christen, J. J.; Rytting, J. H. *Chem. Rev.* **1971**, *71*, 439−481.

(31) Dale, R. M. K.; Martin, E.; Livingston, D. C.; Ward, D. C. *Biochemistry* **1975**, *14*, 2447−2457.

(32) Libera, J. A.; Gurney, R. W.; Schwartz, C.; Jin, H.; Lee, T. L.; Nguyen, S. T.; Hupp, J. T.; Bedzyk, M. J. *J. Phys. Chem. B* **2005**, *109*, 1441−1450.

(33) Puri, S.; Chand, B.; Mehta, D.; Garg, M. L.; Singh, N.; Trehan, P. N. *At. Data Nucl. Data Tables* **1995**, *61*, 289−311.

(34) Bedzyk, M. J.; Bilderback, D.; White, J.; Abruna, H. D.; Bommarito, M. G. *J. Phys. Chem.* **1986**, *90*, 4926−4928.

(35) Parratt, L. G. *Phys. Rev.* **1954**, *95*, 359−369.

(36) Libera, J. A. In situ X-ray structural analysis of polynucleotide surface adsorption and metal-phosphonate self-assembled multilayers. Ph.D. Thesis, Northwestern University, 2005.

(37) Zhuravlev, L. T. *Langmuir* **1987**, *3*, 316−318.

(38) Inside the Si/Mo multilayer mirror, the XSW period $D = d/m$ for the mth-order Bragg peak. Due to strong refraction effects at these small incident angles the XSW period is significantly smaller above the surface than below the surface.

(39) The significantly higher than expected Hg total densities and bulk concentrations for the first X-ray spot at the first two scans is presumably due to a localized Hg-poly(U) precipitate.

(40) Lupis, C. H. P. *Chemical Thermodynamics of Materials*; North-Holland: New York, 1983.

(41) Belloni, L. *Colloids Surf. A* **1998**, *140*, 227−243.

(42) Manning, G. S. *J. Chem. Phys.* **1969**, *51*, 924−933.

(43) Gonzalez-Mozuelos, P.; Olvera de la Cruz, M. *J. Chem. Phys.* **1995**, *103*, 3145−3157.

(44) Iler, R. K. *The Chemistry of Silica*: *Solubility*, *Polymerization*, *Colloid and Surface Properties*, *and Biochemistry*; Wiley: New York, 1979; Chapter 6.

(45) Stumm, W.; Hohl, H.; Dalang, F. *Croat. Chem. Acta* **1976**, *48*, 491−504.

(46) Yates, D. E.; Levine, S.; Healy, T. W. *J. Chem. Soc.*, *Faraday Trans.* **1974**, *170*, 1807−1818.

(47) Fang, F.; Szleifer, I. *J. Chem. Phys.* **2003**, *119*, 1053−1065.

(48) Joanny, J.-F. *Eur. Phys. J. B* **1999**, *9*, 117−122.

(49) Shafir, A.; Andelman, D. *Phys. Rev. E* **2004**, *70*, 061804.

(50) Angelini, T. E.; Sanders, L. K.; Liang, H. J.; Wriggers, W.; Tang, J. X.; Wong, G. C. L. *J. Phys. Condens. Matter* **2005**, *17*, 1123−1135.